

# Super-hard X-Ray Emission from $\eta$ Carinae Observed with Suzaku

Akiko SEKIGUCHI,<sup>1,2</sup> Masahiro TSUJIMOTO<sup>1,3\*</sup> Shunji KITAMOTO<sup>4</sup>, Manabu ISHIDA<sup>1</sup>, Kenji HAMAGUCHI<sup>5,6</sup>,  
Hideyuki MORI<sup>1</sup>, and Yohko TSUBOI<sup>7</sup>

<sup>1</sup>*Japan Aerospace Exploration Agency, Institute of Space and Astronautical Science,  
3-1-1 Yoshino-dai, Sagami-hara, Kanagawa 229-8510*

<sup>2</sup>*School of Physical Science, Space and Aeronautical Science, The Graduate University for Advanced Studies  
Hayama-cho, Miura-gun, Kanagawa 240-0193  
sekiguti@astro.isas.jaxa.jp*

<sup>3</sup>*Department of Astronomy & Astrophysics, Pennsylvania State University,  
525 Davey Laboratory, University Park, PA 16802, USA*

<sup>4</sup>*Department of Physics, Rikkyo University, 3-34-1 Nishi-Ikebukuro, Toshima-ku, Tokyo 171-8501*

<sup>5</sup>*CRESST and X-ray Astrophysics Laboratory NASA Goddard Space Flight Center, Greenbelt, MD 20771, USA*

<sup>6</sup>*Department of Physics, University of Maryland, Baltimore County, 1000 Hilltop Circle, Baltimore, MD 21250, USA*

<sup>7</sup>*Department of Science and Engineering, Chuo University, 1-13-27 Kasuga, Bunkyo-ku, Tokyo 112-8551*

(Received 2022 March 25; accepted 0 0)

## Abstract

We present the Suzaku results of  $\eta$  Carinae in the 5–50 keV range conducted twice around the apastron in 2005 August for 50 ks and in 2006 February for 20 ks. The X-ray Imaging Spectrometer (XIS) produced hard (5–12 keV) band spectra, resolving K shell lines from highly ionized Fe and Ni. The Hard X-ray Detector yielded a significant detection in the super-hard (15–50 keV) band, which is uncontaminated by near-by sources. We constrained the temperature of the optically-thin thermal plasma emission dominant in the hard band as 3–4 keV using the K-shell line features with the XIS. We found significant excess emission above the thermal emission in the super-hard band with the PIN, confirming the previous INTEGRAL ISGRI report. The entire 5–50 keV spectra were fitted by a combination of a thermal plasma model plus a flat power-law or a very hot thermal bremsstrahlung model for the excess emission. No significant change of the excess emission was found at different epochs within the systematic and statistical uncertainties and no flare-like flux amplification was seen in the hard band, indicating that the excess emission is a steady phenomenon. We argue that the super-hard emission is attributable to the inverse Compton of stellar UV photons by non-thermal electrons or to the thermal bremsstrahlung of very hot plasma, and not to the bremsstrahlung by non-thermal electrons colliding with cold ambient matter.

**Key words:** stars: binaries: general — stars: early-type — stars: individual ( $\eta$  Carinae) — X-rays: stars

## 1. Introduction

Colliding wind binaries (CWBs), a binary system comprised of two early-type stars with stellar winds at high mass loss rates and velocities, are the brightest class of stellar hard X-ray emitters. Theoretical interpretations are given for their luminous hard X-rays as the thermal emission from high-temperature plasma produced by strong shocks due to the colliding winds (Luo et al. 1990; Stevens et al. 1992; Usov 1992). The interpretation is supported by the X-ray modulation observed along the orbital motion in some CWBs (Stevens et al. 1996; Ishibashi et al. 1999; Zhekov & Skinner 2000).

CWBs are also expected to be an agent of cosmic particle acceleration, which is evidenced by the presence of non-thermal radio emission from e. g., WR 140 (White & Becker 1995). Charged particles with an energy distribution deviating from the Maxwellian distribution give rise

to the X-ray emission harder than the thermal emission dominant below 10 keV, thus the presence and the process of particle acceleration in CWBs can be best studied in the super-hard X-ray band. For convenience, we refer to the 5–12 keV range as “hard” X-ray band, while the >15 keV range as “super-hard” X-ray band.

The investigation of the super-hard emission from CWBs is important to unveil their enigmatic nature, and possibly gives a clue to understand the origin of  $\gamma$ -ray emission reported from some massive star clusters containing CWBs (Aharonian et al. 2007). We anticipate a great leap in our comprehension of non-thermal phenomena in CWBs with the advent of X-ray imaging telescopes in the super-hard band, which will be deployed in the next generation X-ray satellites such as Astro-H (Takahashi et al. 2008). At present, however, our tool is limited to non-imaging or coded-mask techniques in this band, leaving  $\eta$  Carina the only practical target for this subject.

$\eta$  Car is a luminous blue variable in the Carina nebula at a distance of 2.3 kpc (Davidson & Humphreys 1997).

\* Chandra Fellow

**Table 1.** Observation log.

Number	Sequence number	Observation start		Observation end		Exposure (ks)		Orbital phase*
		Date	Time	Date	Time	XIS	HXD	
First	100012010	2005-08-29	01:48	2005-08-30	01:30	50	53	1.39
Second	100045010	2006-02-03	09:59	2006-02-03	22:45	21	17	1.47

\* The orbital phase 1.0 indicates the onset of the Cycle 11 minimum at the Julian date 2452819.8 d (Damineli et al. 2008).

It is considered to constitute a binary system with another massive star with an orbital period of  $2022.7 \pm 1.3$  d (Damineli et al. 2008) in a highly eccentric orbit (Nielsen et al. 2007). In this paper, we use the orbital phase such that the start of the Cycle 11 minimum is phase 1.0 on the Julian date of 2452819.8 d (Damineli et al. 2008) or 2003 June 29.3.  $\eta$  Car is one of the brightest stellar hard X-ray sources, and the hard X-ray modulation along the proposed ephemeris endorses the colliding-wind origin of the emission (Ishibashi et al. 1999).

The development of the X-ray light curve through an orbital phase is as follows; it experiences an eclipse from phase 0 to 0.03 (we call “minimum”), recovers its brightness spending  $\sim 0.02$  phases (“recovery”), and gradually increases the flux for the rest of the phase (“steady increase”) to reach the brightest point (“maximum”), which is terminated by the repeated eclipse in the next phase (Ishibashi et al. 1999; Pittard & Corcoran 2002). The periastron and the apastron are supposed to occur around phase 0.0 and 0.5, respectively (e.g., Fernández-Lajús et al. 2009). During the development,  $\eta$  Car shows episodic flares (Ishibashi et al. 1999; Hamaguchi et al. 2007a). The spectrum of  $\eta$  Car below 10 keV has been described by complex models comprised of several thin-thermal plasma components with different temperatures, but a single plasma component of a 3–4 keV temperature dominates the hard band emission (Tsuboi et al. 1997; Corcoran et al. 1998).

X-ray studies of  $\eta$  Car in the super-hard band were conducted by two observatories to date. One is by BeppoSAX using a combination of a gas scintillation proportional counter (MECS; Medium Energy Concentrator Spectrometer) below 10 keV and a non-imaging phoswich scintillators (PDS; Phoswich Detection System) above 15 keV. Viotti et al. (2002) and Viotti et al. (2004) constrained the parameters of the 3–4 keV plasma component using the hard band data by the MECS, and extrapolated the model to claim that the PDS data contain excess emission upon the 3–4 keV thermal emission. The other is by the International Gamma-Ray Astrophysics Laboratory (INTEGRAL) using a coded-mask imager (ISGRI; the INTEGRAL Soft Gamma-Ray Imager) in the 15 keV–1 MeV range. Leyder et al. (2008) unambiguously confirmed the super-hard emission claimed by the BeppoSAX studies, showing that the ISGRI image has a significant signal at the position of  $\eta$  Car.

When it comes to characterizing the spectrum of the super-hard excess emission, the results produced by the two observatories have a limited use with some concerns. The PDS is a non-imaging instrument with a wide field

of view of  $1.3^\circ$  in the full width at the half maximum (FWHM), thus the contamination by other sources is inevitable. Indeed, as was pointed out by Leyder et al. (2008), two neighboring super-hard sources (IGR J10447–6027 and 1E1048.1–5937) are within the PDS field of view, which significantly contribute to the PDS spectrum of  $\eta$  Car. The ISGRI resolved super hard emission from  $\eta$  Car and is free from the contamination by these two sources. However, its spectrum does not have rich statistics with only three spectral bins for a total of a 1 Ms exposure. The flux variation cannot be tested. Also, the excess emission was examined against the extrapolated model of the 3–4 keV thermal emission obtained by the MECS at a different epoch, which may not be very appropriate given the variable nature of the hard X-rays of  $\eta$  Car.

The detection and the characterization of the excess emission in the super-hard band heavily depend on the accurate characterization and subtraction of the 3–4 keV thermal emission. The examination of the excess emission is straight-forward, but it requires a careful treatment since the extrapolation of the 3–4 keV thermal model needs to be stretched for nearly an order of magnitude in the energy range.

With these concerns, it is not surprising that the BeppoSAX and the INTEGRAL data resulted in a serious disagreement with each other for the super-hard excess emission. While the former claims the power-law model of a photon index of  $2.42 \pm 0.04$ , the latter claims  $1 \pm 0.4$ . Moreover, the flux estimates are inconsistent significantly by a factor of 3. It is unclear, in the first place, whether the super-hard excess emission is of a thermal or a non-thermal origin.

To mitigate some of these concerns in the previous studies, we present the 5–50 keV results of Suzaku observations conducted in 2005 August and 2006 February. The non-imaging detector in the super-hard band on board Suzaku has a narrower field of view than that of the PDS and is free from the contamination by the two neighboring super hard sources. The X-ray charge coupled devices (CCDs) sensitive below 12 keV have good and well-calibrated responses in the hard band. Their spectroscopic capability outperforms that of the MECS, resolving emission lines in the Fe and Ni K complex in the 6.0–8.5 keV band and thus enabling an accurate temperature determination of the 3–4 keV plasma sufficient to extrapolate toward the super-hard band.

We present the spectral models to explain the 5–50 keV emission of  $\eta$  Car at two epochs around the apastron. We examine the thermal or non-thermal nature of the super

hard excess emission and investigate its flux variability. The results will set a firm basis to study the development of the super-hard emission in an entire orbital cycle, which we plan to conduct in a separate paper with the new data obtained at the end of 2008 during the latest X-ray maximum and minimum.

## 2. Observations and Data Reduction

The Suzaku satellite (Mitsuda et al. 2007) observed the Carina nebula multiple times since its launch. We present the results of  $\eta$  Car in the first two observations on 2005 August 29 and 2006 February 3 in this paper, during which the object was around the apastron at the orbital phases of 1.39 and 1.47, respectively (table 1). The two observations were centered at (RA, Dec) = ( $10^{\text{h}}45^{\text{m}}03^{\text{s}}.6$ ,  $-59^{\circ}41'04''$ ) in the equinox J2000.0 with nearly the opposite position angles. Using the first data set, Hamaguchi et al. (2007b) studied the soft diffuse emission around  $\eta$  Car.

Suzaku has a low earth orbit with an altitude of  $\sim 570$  km. The observatory has two working instruments; the X-ray Imaging Spectrometer (XIS; Koyama et al. 2007) and the Hard X-ray Detector (HXD; Takahashi et al. 2007; Kokubun et al. 2007), which respectively covers the energy range of 0.2–12 keV and 10–600 keV.

The XIS is an imaging spectrometer using X-ray CCDs with a format of  $1024 \times 1024$  pixels. Four CCD cameras are installed in the focal planes of four X-ray telescope modules (Serlemitsos et al. 2007) coaligned with each other. Three of the four cameras (XIS 0, 2, and 3) are front-illuminated (FI) devices and the remaining one (XIS1) is back-illuminated (BI). The FI and the BI CCDs have superior sensitivity to each other in the hard and the soft bands, respectively. The energy resolution, which is subject to degradation in the orbit, is  $\sim 140$  eV and  $\sim 160$  eV at 5.9 keV in FWHM respectively for the first and the second observations. The absolute energy gain is accurate to  $\sim 0.2\%$  at 5.9 keV. Together with the XRT, the XIS covers a field of view of  $18' \times 18'$  with a pixel scale of  $1''$  pixel $^{-1}$ . The half-power diameter of the XRT is  $1/8$ – $2/3$ , which is almost independent of energy.

The HXD is a non-imaging spectrometer, consisting of several components responsible for different energy ranges. In this paper, we use the PIN component sensitive at 10–70 keV with an FWHM energy resolution of 3.0 keV. The PIN detector is composed of 64 Si PIN diodes installed at the bottom of  $8 \times 8$  well-type collimators surrounded by GSO scintillators. The fine collimators within each well restrict the field of view. The effective area monotonically decreases as an increasing distance from the field center, which is characterized by the FWHM view of  $\sim 34'$  or the full width at zero intensity (FWZI) view of  $70'$  square (figure 1). The center of the PIN field is  $3/5$  offset from that of the the XIS field. Thanks to the surrounding anti-coincidence scintillators, the narrow field of view, and the low background environment in the orbit, the PIN achieves unprecedented sensitivity in the super-hard band.

In both observations, the XIS is operated in the normal clocking mode with a frame time of 8 s. We used the cleaned event lists produced by the pipeline processing version 2.0. The net exposure times are compiled in table 1. We used the HEASoft version 6.5.1<sup>1</sup> for the data reduction and Xspec version 11.3.2<sup>2</sup> for the X-ray spectral analysis.

## 3. Analysis

### 3.1. Constructing the Spectra

#### 3.1.1. XIS

Figure 1 (b) shows the XIS image in the first observation. Three point sources are recognized besides  $\eta$  Car: HD 93250, HD 93205, and WR 25, all of which are massive stars in this region. The underlying diffuse emission, which is a combination of unresolved point sources and the soft extended emission (Evans et al. 2003; Evans et al. 2004; Albacete Colombo et al. 2003; Hamaguchi et al. 2007b), is noticeable particularly in the western half of the image. The second observation produced a similar image.

In order to construct the XIS spectra, we extracted the source and the background events from the solid and the dashed circles in figure 1 (b), respectively. The source extraction region is a  $3'$  radius circle containing  $\sim 95\%$  of photons from a point-like source at the circle center. The background region is selected from a region devoid of bright emission. The pile-up is negligible. The wings of other point sources and the underlying diffuse emission contribute to the background, which is negligible in our targeted energy range. This is illustrated by the fact that the emission above 5 keV at the X-ray minimum of  $\eta$  Car, which gives the upper limit to the contamination by irrelevant emission, is roughly two orders of magnitude smaller than that in the X-ray bright phase (Hamaguchi et al. 2007a).

We constructed hard band light curves of the count rate during the 50 and 21 ks exposures in the first and the second observations, respectively, and found no significant flux changes such as flare-like variability (figure 2). For the spectral modeling, we merged the spectra obtained by the three FI devices with nearly identical responses. The merged FI spectrum has a good signal up to  $\sim 12$  keV, while the BI spectrum is effective up to  $\sim 9$  keV. We generated the redistribution matrix functions and the ancillary response files using the `xisrmfgen` and `xissimarfgen` tools (Ishisaki et al. 2007), respectively.

#### 3.1.2. PIN

Figure 1 (a) shows the field of view of the PIN detector. One of the two INTEGRAL sources (IGR J10447–6027) is outside of the FWZI view. The other (1E 1048.1–5937) is close to the edge of the view in both observations, at which the effective area decreases to less than 5% of the value at the field center. Leyder et al. (2008) claimed the INTEGRAL ISGRI count rate of  $0.16 \text{ s}^{-1}$  for  $\eta$  Car and

<sup>1</sup> See <http://heasarc.gsfc.nasa.gov/docs/software/lheasoft/> for detail.

<sup>2</sup> See <http://heasarc.gsfc.nasa.gov/docs/xanadu/xspec/index.html> for detail.

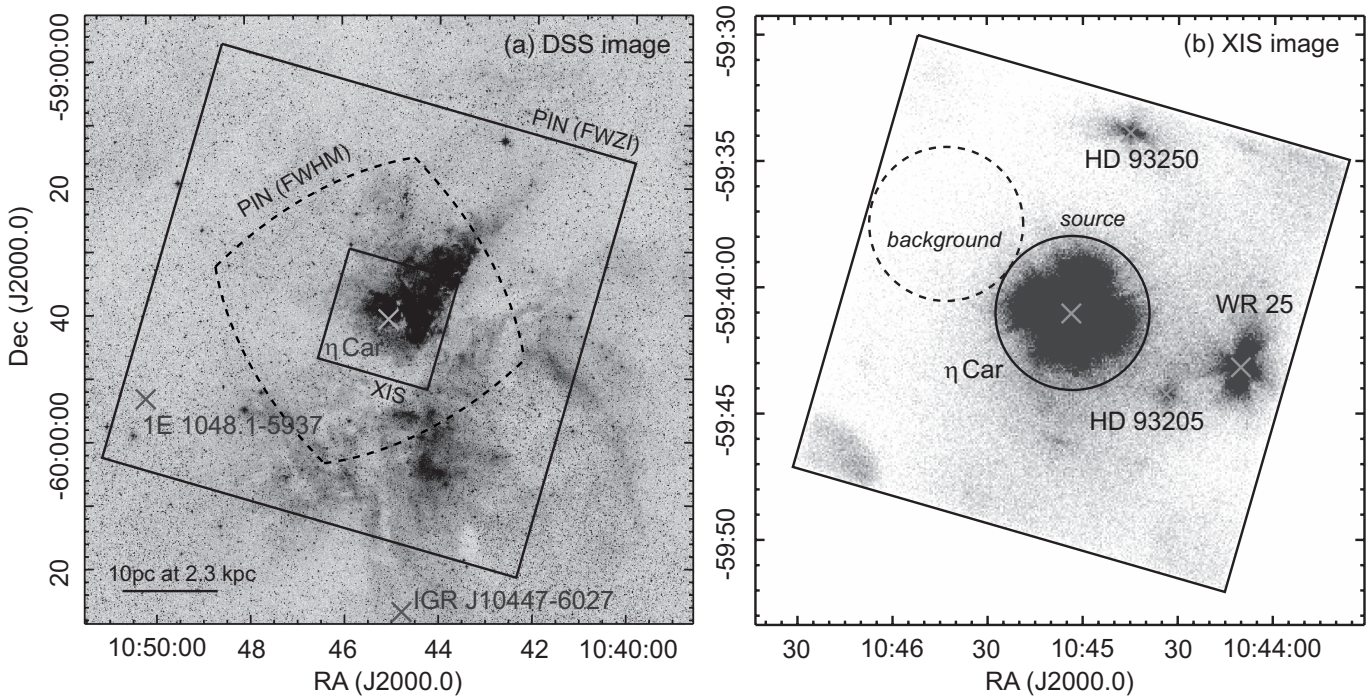


**Fig. 1.** (a) Fields of view of the XIS (small solid square) and the PIN (large solid square for FWZI and dashed region for FWHM) in the first observation overlaid on an optical image by the Digitized Sky Survey around  $\eta$  Car. The positions of the INTEGRAL super-hard sources are shown (Leyder et al. 2008) with crosses. (b) XIS image in the first observation. The events obtained by the four CCDs are merged. The positions and the names of  $\eta$  Car and the neighboring resolved bright X-ray sources are labeled. The solid and the dashed circles represent the source and the background extraction regions, respectively. The X-ray events in the corners stem from the calibration sources.

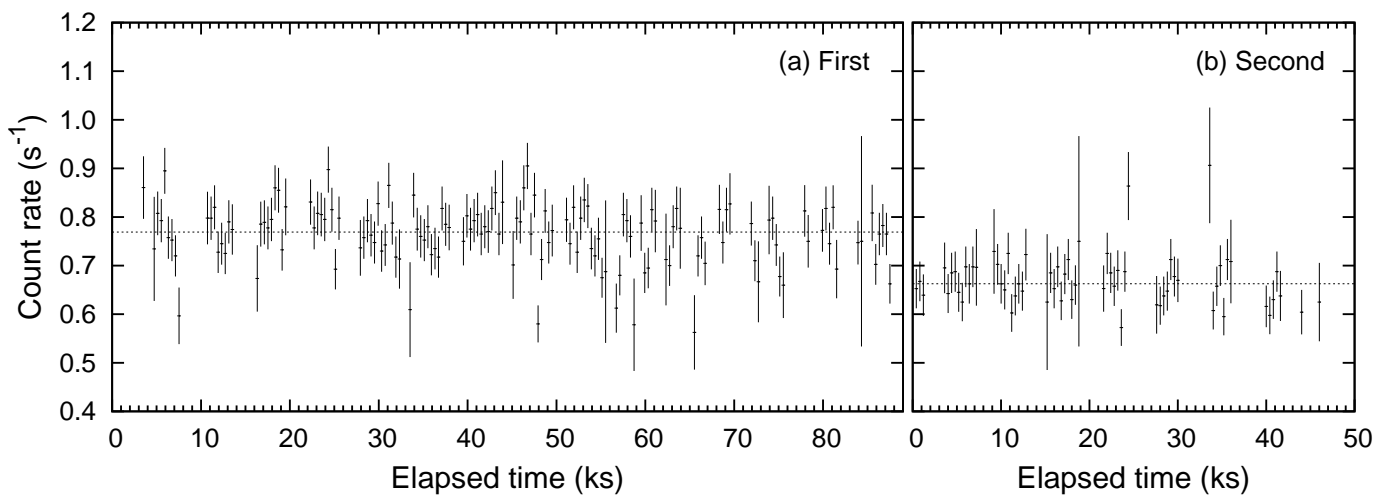


**Fig. 2.** XIS 5–10 keV light curve binned with  $400 s \text{ bin}^{-1}$  in (a) the first and (b) the second observations. The best-fit constant model is shown with the dashed lines. The origin of the abscissa is the start of the observation.

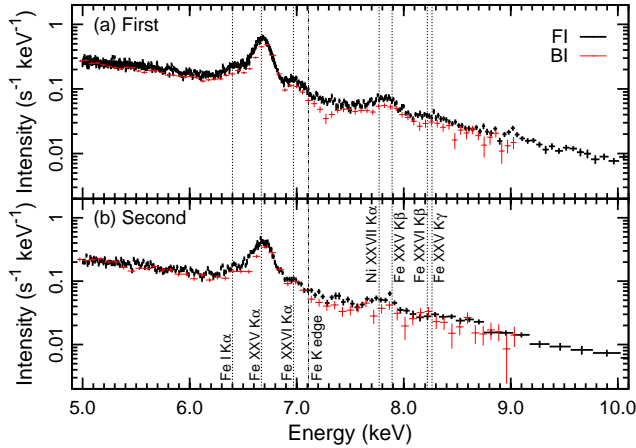


**Fig. 3.** XIS spectra in the 5–10 keV range in (a) the first and (b) the second observations. The FI and BI spectra are shown with black and red error bars, respectively, with bold face symbols for the FI spectra. The conspicuous emission lines as well as the Fe K edge are labeled.

$0.09 \text{ s}^{-1}$  for 1E 1048.1–5937. Assuming that 1E 1048.1–5937 does not vary drastically among the INTEGRAL and the two Suzaku observations, the contamination by this source is negligible in the PIN spectrum.

We constructed the background spectrum, which is composed mostly of the non X-ray background (NXB) with some contribution by the Cosmic X-ray Background (CXB). The Galactic Ridge X-ray emission is negligible toward  $\eta$  Car at a galactic longitude of  $\sim 290^\circ$ . For the NXB, we used the simulated background events distributed by the instrument team, which reproduces the NXB spectrum at an accuracy of 1.3%<sup>3</sup>. For the CXB, we assumed the spectral model derived from HEAO-1 observations (Boldt 1987). We produced a CXB spectrum by convolving the detector angular and energy responses with the simulated emission of the assumed model and the spatially uniform distribution. The resultant NXB and CXB data were merged to construct the PIN background spectrum.

For the spectral modeling, we used the latest detector response for a point source at the XIS field center (`ae_hxd_pinxinome1_20080129.rsp`). At this position, the relative flux among the XIS devices and the PIN is calibrated at an accuracy of  $\sim 1\%$ <sup>4</sup>.

### 3.2. Modeling the Spectra

#### 3.2.1. Fitting below 10 keV

With the background-subtracted spectra and the response files both for the XIS and the PIN, we are now ready for the spectral modeling. It is not a wise decision to start fitting the two spectra simultaneously; the statistics of the XIS spectrum overwhelms that of the PIN

**Table 2.** Best-fit model for 6.0–8.5 keV spectra.

Parameters*	First <sup>†</sup>	Second <sup>†</sup>
$k_B T^{(\text{th})}$ (keV)	$3.9^{+0.1}_{-0.1}$	$4.1^{+0.3}_{-0.3}$
$Z_{\text{Fe}}^{(\text{th})}$ (solar)	$0.47^{+0.01}_{-0.02}$	$0.45^{+0.02}_{-0.03}$
$Z_{\text{Ni}}^{(\text{th})}$ (solar)	$1.4^{+0.2}_{-0.2}$	$0.9^{+0.4}_{-0.4}$
$F_X^{(\text{th})}$ ( $10^{-11} \text{ erg s}^{-1} \text{ cm}^{-2}$ )	$2.90^{+0.02}_{-0.03}$	$2.23^{+0.03}_{-0.12}$
$E^{(\text{gau})}$ (keV)	$6.42^{+0.01}_{-0.01}$	$6.43^{+0.01}_{-0.01}$
$I^{(\text{gau})}$ ( $10^{-5} \text{ s}^{-1} \text{ cm}^{-2}$ )	$8.5^{+0.6}_{-0.6}$	$6.1^{+0.9}_{-0.9}$
$E^{(\text{edge})}$ (keV)	$7.11^{+0.07}_{-0.06}$	$6.97^{+0.15}_{-0.10}$
$\tau^{(\text{edge})}$	$0.12^{+0.03}_{-0.03}$	$0.12^{+0.08}_{-0.04}$
$\chi^2/\text{d.o.f.}$	346.2/323	143.9/138

\* The superscripts of the parameters represent the spectral component that they belong to: “(th)” for the thin-thermal plasma, “(gau)” for the Gaussian line, and “(edge)” for the photoelectric absorption model.  $F_X^{(\text{th})}$  is derived in 5–10 keV.

<sup>†</sup> The best-fit values for the first and the second observations. The ranges indicate the 90% statistical uncertainty.

spectrum, making the PIN data ignored when fitted at the equal weight. We therefore took a more step-wise approach described below.

Figure 3 shows the XIS spectra in the 5–10 keV range, in which we can resolve emission lines from highly ionized Fe and Ni as well as hard continuum emission extending beyond 10 keV. These are the characteristics of the emission arising from a thin-thermal plasma of several keV temperatures. In addition to the thermal features, we can also find an emission line at  $\sim 6.4$  keV due to the  $K\alpha$  emission of quasi-neutral Fe (hereafter called Fe I) and an absorption feature at 7–8 keV due to the K-shell photoelectric absorption edge by Fe I.

The rich set of thermal features in our XIS spectra enables us to constrain the plasma temperature stringently, in particular, by using the intensity ratio between the Fe XXV  $K\alpha$  line at 6.7 keV and Fe XXV  $K\beta$  line at 7.9 keV and that between Fe XXV  $K\alpha$  line at 6.7 keV and Fe XXVI  $K\alpha$  line at 7.0 keV.

To fully exploit the XIS capability, we fitted the 6.0–8.5 keV range spectra, in which we can find most of the emission lines responsible for the plasma temperature determination. We applied the model composed of a thin-thermal plasma component (`vmekal`; Mewe et al. 1985; Mewe et al. 1986; Kaastra 1992; Liedahl et al. 1995) for the thermal features and a Gaussian line component for the Fe I  $K\alpha$  line. We attenuated the model by an interstellar extinction model (`wabs`; Morrison & McCammon 1983) as well as an additional photoelectric absorption edge to account for the Fe K edge feature. The free parameters in the fitting are the plasma temperature ( $k_B T^{(\text{th})}$ ), the Fe and Ni abundance ( $Z_{\text{Fe}}^{(\text{th})}$  and  $Z_{\text{Ni}}^{(\text{th})}$ , respectively), and the flux ( $F_X^{(\text{th})}$ ) in the 5–10 keV band for the thin-thermal plasma component, the line energy ( $E^{(\text{gau})}$ ) and the intensity ( $I^{(\text{gau})}$ ) for the Gaussian line component, and the edge energy ( $E^{(\text{edge})}$ ) and the optical depth ( $\tau^{(\text{edge})}$ ) for the photoelectric absorption edge component. Here,

<sup>3</sup> See <http://www.astro.isas.jaxa.jp/suzaku/doc/suzakumemo/suzakumemo-2008-03.pdf> and <http://heasarc.gsfc.nasa.gov/docs/suzaku/analysis/pinbgd.html> for detail.

<sup>4</sup> See <http://www.astro.isas.jaxa.jp/suzaku/doc/suzakumemo/suzakumemo-2007-11.pdf> for detail.

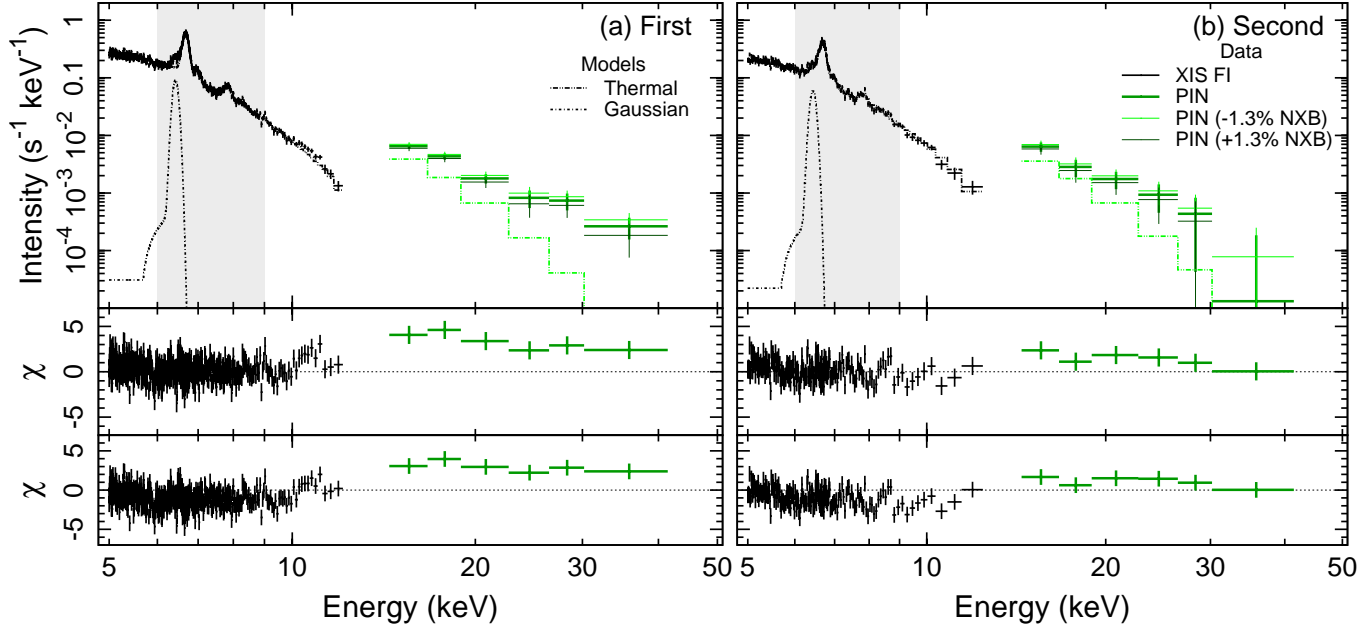


**Fig. 4.** 5–50 keV spectrum compared to the best-fit model for the 6.0–8.5 keV (the gray shaded range) spectrum in (a) the first and (b) the second observations. The top panels show the data and each spectral component of the model (see the legend in the top left panel). For the XIS spectra, we plot only the FI spectrum. For the PIN spectra, three spectra are shown with different darkness of green colors. Each represents the data constructed with three NXB models; i. e., the distributed model and its scaled models by the systematic uncertainty of  $\pm 1.3\%$  (see the legend at the top right panel). The middle panels show the residuals of the data from the best-fit 6.0–8.5 keV model. The bottom panels show the residuals of the data from the model using the maximum allowed values of  $k_{\text{B}}T^{(\text{th})}$  and  $F_{\text{X}}^{(\text{th})}$  of the best-fit 6.0–8.5 keV model (table 2).

the superscripts of the parameters represent the spectral component that they belong to. The amount of extinction was fixed to  $1.7 \times 10^{23} \text{ cm}^{-2}$ , which is a typical value derived in the hard band for the colliding-wind plasma of  $\eta$  Car (Hamaguchi et al. 2007a). The intrinsic width of the Gaussian line was fixed to 0 eV. The linearity coefficient between the pulse height and the energy was adjusted to compensate for a possible systematic uncertainty.

We obtained statistically-acceptable fits both for the first and the second observations (table 2). The plasma temperature ( $k_{\text{B}}T^{(\text{th})}$ ) and the flux ( $F_{\text{X}}^{(\text{th})}$ ) were determined at an accuracy of  $\sim 5\%$ . The flux between the two observations changed significantly by  $\sim 20\%$ . It is interesting to note that, while  $Z_{\text{Fe}}^{(\text{th})}$  and  $Z_{\text{Ni}}^{(\text{th})}$  are consistent between the two observations,  $Z_{\text{Ni}}^{(\text{th})}$  is larger than  $Z_{\text{Fe}}^{(\text{th})}$  by a factor of a few; its cause is not clear.

### 3.2.2. Extending beyond 10 keV

We extrapolated the best-fit 6.0–8.5 keV model beyond 10 keV and compared to the PIN spectrum in order to examine the excess emission in the super-hard band. The top panels in figure 4 show the XIS and the PIN spectra below 12 keV and above 15 keV, respectively, in comparison with the extrapolated best-fit model in the 6.0–8.5 keV range. The middle panels show the residuals, in which we can see a consistent positive residual for the PIN spectrum in both observations. This illustrates the presence of the excess emission beyond 15 keV.

We tested the claim for two major sources of systematic uncertainty. One is the systematic uncertainty in the NXB model of the PIN data, which constitutes the majority of the background signal. We constructed the background-subtracted PIN spectra for the scaled NXB models by  $\pm 1.3\%$ , which is the accuracy of the model, and plotted them against the extrapolated model in different darkness of green colors in the top panels of figure 4. For the increased NXB model, we still find consistent positive residuals beyond 10 keV. The other is the statistical uncertainty in the best-fit 6.0–8.5 keV model. In order to examine the upper bound of the extrapolated model, we replaced the best-fit  $k_{\text{B}}T^{(\text{th})}$  and  $F_{\text{X}}^{(\text{th})}$  values with their maximum allowed values within 90% statistical uncertainty. The modified model was extrapolated and compared to the data. The residuals are shown in the bottom panels in figure 4, which again show consistent positive residuals of the data above the extrapolated model.

### 3.2.3. Fitting the Entire Band

We established the presence of the excess emission in the super-hard band and now proceed to the spectral modeling in the entire 5–50 keV range using both the XIS and the PIN data. For the hard emission, we used the same model for the 6.0–8.5 keV fitting procedure in subsection 3.2.1 with a slight modification that the  $Z_{\text{Fe}}^{(\text{th})}$  and  $Z_{\text{Ni}}^{(\text{th})}$  are tied between the two observations. Upon

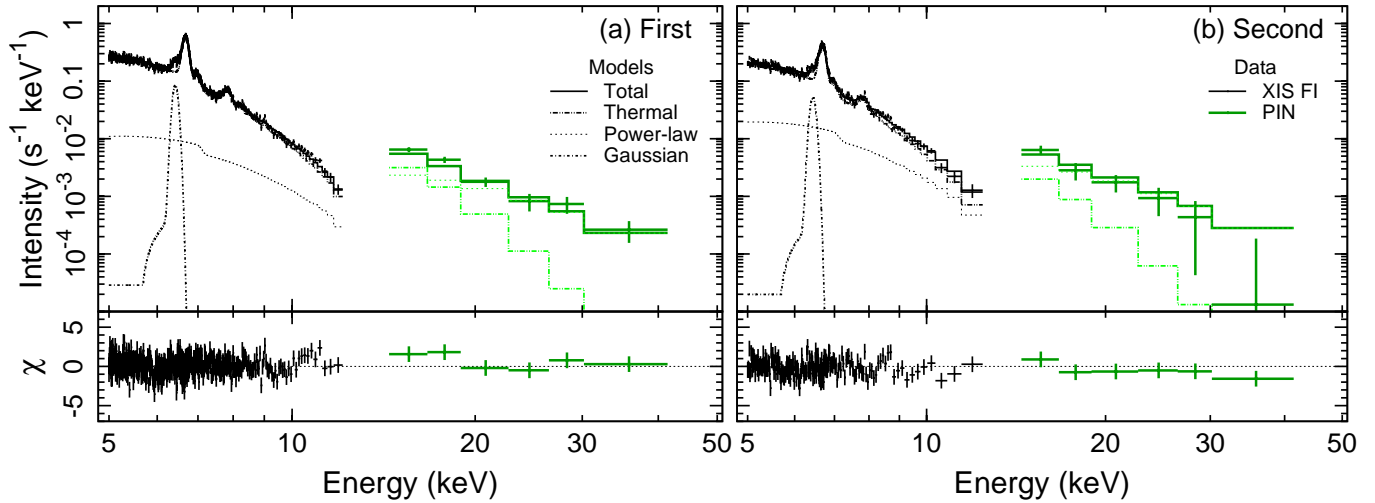


Fig. 5. 5–50 keV spectrum and the best-fit model. A power-law model is added to explain the super-hard excess emission. The top panels show the data and the best-fit spectra and their components (see the legend in the top left panel). XIS FI and PIN data are shown with black and green colors, respectively. The best-fit parameters of the models are compiled in table 3.

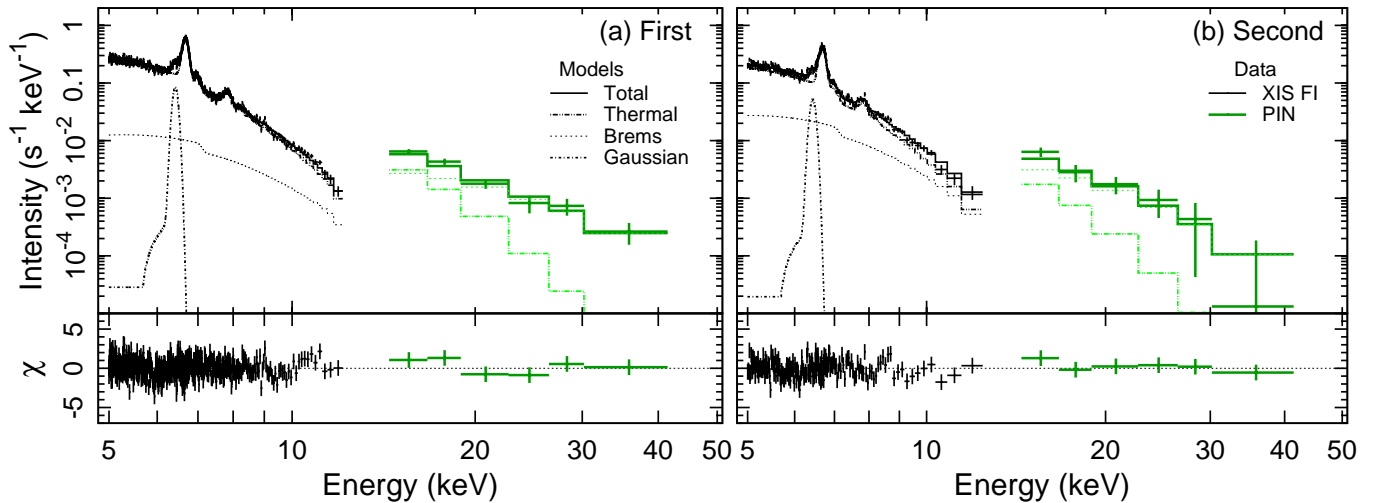


Fig. 6. 5–50 keV spectrum and the best-fit model. A thermal bremsstrahlung model is added to explain the super-hard excess emission. The symbols and colors follow figure 5. The best-fit parameters of the models are compiled in table 4.

this thermal emission, we added another component to account for the super-hard excess emission. Two models were employed; a power-law model and a thermal bremsstrahlung. The free parameters in the additional components are the power-law photon index ( $\Gamma^{(pl)}$ ) and the flux  $F_X^{(pl)}$  in the 10–50 keV range for the power-law model and the electron temperature ( $k_B T^{(br)}$ ) and the 10–50 keV flux ( $F_X^{(br)}$ ) for the bremsstrahlung model. Both yielded an acceptable fit. The best-fit values are tabulated in tables 3 and 4, while the data and the best-fit model are shown in figures 5 and 6, respectively, for the additional power-law and bremsstrahlung models.

We assessed the systematic uncertainty in the derived

parameters for the two major sources of such uncertainty. First, for the PIN NXB model uncertainty, we repeated the 5–50 keV fitting procedure using the scaled NXB models by  $\pm 1.3\%$ . For the power-law model, we found that this brings systematic uncertainties of  $(\Gamma, F_X^{(pl)}/10^{-11} \text{ erg s}^{-1} \text{ cm}^{-2}) \sim (0.2, 0.3)$  for the first and  $(0.1, 0.3)$  for the second observations. For the bremsstrahlung model, the systematic uncertainty for  $F_X^{(br)}/10^{-11} \text{ erg s}^{-1} \text{ cm}^{-2}$  is  $\sim 0.6$  and  $\sim 0.5$  in the first and the second observations, respectively. The resultant systematic uncertainty of  $k_B T^{(bb)}$  is so large that it makes  $k_B T^{(bb)}$  practically unconstrained in the first observation and  $>16$  keV in the second observation. Next,

**Table 3.** Best-fit model for the 5–50 keV spectra using a power-law model for the super-hard excess emission.

Parameters*	First <sup>†</sup>	Second <sup>†</sup>
$\Gamma^{(\text{pl})}$	$1.30^{+0.07}_{-0.14}$	$1.51^{+0.04}_{-0.15}$
$F_X^{(\text{pl})}$ ( $10^{-11}$ erg s $^{-1}$ cm $^{-2}$ )	$1.4^{+0.2}_{-0.1}$	$1.9^{+0.2}_{-0.2}$
$k_B T^{(\text{th})}$ (keV)	$3.61^{+0.03}_{-0.03}$	$3.29^{+0.03}_{-0.03}$
$Z_{\text{Fe}}^{(\text{th})}$ (solar)	$0.47^{+0.01}_{-0.01}$	
$Z_{\text{Ni}}^{(\text{th})}$ (solar)	$1.5^{+0.2}_{-0.2}$	
$F_X^{(\text{th})}$ ( $10^{-11}$ erg s $^{-1}$ cm $^{-2}$ )	$2.76^{+0.02}_{-0.01}$	$2.07^{+0.02}_{-0.02}$
$E^{(\text{gau})}$ (keV)	$6.43^{+0.01}_{-0.01}$	$6.44^{+0.01}_{-0.02}$
$I^{(\text{gau})}$ ( $10^{-5}$ s $^{-1}$ cm $^{-2}$ )	$7.9^{+0.5}_{-0.5}$	$5.5^{+0.8}_{-0.7}$
$E^{(\text{edge})}$ (keV)	$7.12^{+0.04}_{-0.04}$	$7.14^{+0.17}_{-0.10}$
$\tau^{(\text{edge})}$	$0.16^{+0.02}_{-0.02}$	$0.14^{+0.04}_{-0.04}$
$\chi^2/\text{d.o.f.}$	717.0/590	286.1/226

\* The superscripts of the parameters represent the spectral component that they belong to: “(pl)” for the power-law, “(th)” for the thin-thermal plasma, “(gau)” for the Gaussian line, and “(edge)” for the photoelectric absorption model.  $F_X^{(\text{th})}$  is derived in 5–10 keV, while  $F_X^{(\text{pl})}$  is in 10–50 keV.

<sup>†</sup> The best-fit values for the first and the second observations. The ranges indicate the 90% statistical uncertainty.

for the statistical uncertainty in the best-fit 3–4 keV thermal model parameters, we replaced the best-fit set of  $k_B T^{(\text{th})}$  and  $F_X^{(\text{th})}$  values with those of their maximum and minimum allowed values within 90% statistical uncertainty. This brings systematic uncertainties of ( $\Gamma$ ,  $F_X^{(\text{pl})}/10^{-11}$  erg s $^{-1}$  cm $^{-2}$ )  $\sim$  (0.02, 0.2) and (0.01, 0.2) respectively for the first and the second observations in the power-law model. For the bremsstrahlung model, the  $k_B T^{(\text{bb})}$  keV is unconstrained with minima of >22 keV and >10 keV for the first and the second observations. The resultant systematic uncertainty for  $F_X^{(\text{bb})}/10^{-11}$  erg s $^{-1}$  cm $^{-2}$  is 0.3 and 0.2, respectively.

## 4. Discussion

### 4.1. Comparison with the Previous Results

We compare the results for the super-hard excess emission among the two Suzaku observations and the two previous studies. We use the spectral parameters for the power-law model, which are available both for the BeppoSAX and the INTEGRAL results (table 5). The flux values of BeppoSAX (Viotti et al. 2004) and Suzaku (table 3) were reevaluated in the 22–100 keV range to facilitate comparison with the INTEGRAL result (Leyder et al. 2008).

We see no significant change between the two Suzaku results both for the flux and the power-law index if we consider both the statistical and systematic uncertainties. Therefore, we fitted the two 5–50 keV spectra simultaneously to obtain a much constrained fit. In the fitting, the best-fit parameters of the thin-thermal plasma components were fixed to the best-fit values for the independent fits. The parameters of the statistically-acceptable best fit are appended in table 5.

The Suzaku results were obtained at different epochs

**Table 4.** Best-fit model for the 5–50 keV spectra using a thermal bremsstrahlung model for the super-hard excess emission.

Parameters*	First <sup>†</sup>	Second <sup>†</sup>
$k_B T^{(\text{br})}$ (keV)	> 61	$18^{+20}_{-8}$
$F_X^{(\text{br})}$ ( $10^{-11}$ erg s $^{-1}$ cm $^{-2}$ )	$1.7^{+0.5}_{-0.4}$	$1.2^{+0.9}_{-0.8}$
$k_B T^{(\text{th})}$ (keV)	$3.58^{+0.07}_{-0.11}$	$3.14^{+0.28}_{-0.14}$
$Z_{\text{Fe}}^{(\text{th})}$ (solar)	$0.47^{+0.01}_{-0.01}$	
$Z_{\text{Ni}}^{(\text{th})}$ (solar)	$1.5^{+0.2}_{-0.2}$	
$F_X^{(\text{th})}$ ( $10^{-11}$ erg s $^{-1}$ cm $^{-2}$ )	$2.74^{+0.10}_{-0.12}$	$1.95^{+0.11}_{-0.18}$
$E^{(\text{gau})}$ (keV)	$6.43^{+0.01}_{-0.01}$	$6.43^{+0.01}_{-0.02}$
$I^{(\text{gau})}$ ( $10^{-5}$ s $^{-1}$ cm $^{-2}$ )	$7.8^{+0.3}_{-0.5}$	$5.3^{+0.8}_{-0.8}$
$E^{(\text{edge})}$ (keV)	$7.12^{+0.06}_{-0.04}$	$7.1^{+0.2}_{-0.1}$
$\tau^{(\text{edge})}$	$0.16^{+0.04}_{-0.03}$	$0.14^{+0.08}_{-0.06}$
$\chi^2/\text{d.o.f.}$	714.1/590	276.2/226

\* The superscripts of the parameters represent the spectral component that they belong to: “(br)” for the bremsstrahlung, “(th)” for the thin-thermal plasma, “(gau)” for the Gaussian line, and “(edge)” for the photoelectric absorption model.  $F_X^{(\text{th})}$  is derived in 5–10 keV, while  $F_X^{(\text{br})}$  is in 10–50 keV.

<sup>†</sup> The best-fit values for the first and the second observations. The ranges indicate the 90% statistical uncertainty or the lower limit.  $k_B T^{(\text{br})}$  is unconstrained in the first observation.

**Table 5.** Comparison with previous results.

Observatory	$\Gamma^{*\dagger}$	$F_X^{*\dagger}/10^{-11}$ (erg s $^{-1}$ cm $^{-2}$ )	Orbital phase <sup>‡</sup>
BeppoSAX	$2.42^{+0.04}_{-0.04}$	3.24	0.46
INTEGRAL	$1.0^{+0.4}_{-0.4}$	$1.11 \pm 0.15$	0.98–1.36
Suzaku (1st)	$1.30^{+0.07}_{-0.14}$	$2.7^{+0.2}_{-0.3}$	1.39
Suzaku (2nd)	$1.51^{+0.04}_{-0.15}$	$1.9^{+0.3}_{-0.1}$	1.47
Suzaku (both)	$1.38^{+0.14}_{-0.13}$	$2.3^{+0.7}_{-0.6}$	1.39, 1.47

\* The best-fit photon index ( $\Gamma$ ) and the flux ( $F_X$ ) in the 22–100 keV range of the power-law model.

<sup>†</sup> The ranges indicate the 90% statistical uncertainty. The uncertainty for the INTEGRAL value was derived from Leyder et al. (2008).

<sup>‡</sup> The orbital phase 1.0 indicates the onset of the Cycle 11 minimum at the Julian date 2452819.8 d (Damineli et al. 2008).

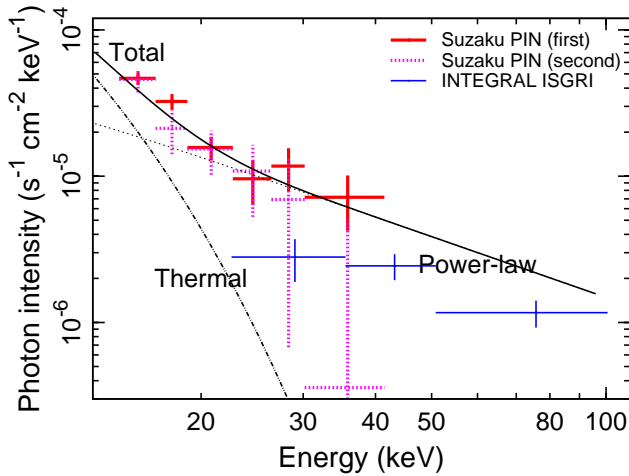


Fig. 7. super-hard spectra by the two Suzaku and the INTEGRAL observations. The best-fit model for the merged Suzaku spectrum is shown (dotted for the power-law, dashed-and-dotted for the thin-thermal, and solid for the total model).

during the X-ray steady increase phase near the apastron with no apparent flare-like flux amplification in the hard band. This infers that the super-hard excess emission is not caused by episodic events, but is a constant emission with little change both in the flux and the spectral hardness.

The best-fit Suzaku model is compared to the INTEGRAL spectrum in figure 7.  $\Gamma$  is the same within the statistical and the systematic uncertainties, but  $F_X$  is significantly higher in Suzaku than INTEGRAL (table 5). The INTEGRAL result was obtained in a wide range of orbital phases including the minimum, recovery, and steady increase by accumulating a 1 Ms exposure. We speculate that the lower flux in the INTEGRAL data is a consequence of the fact that the INTEGRAL spectrum was accumulated in periods including the orbital eclipse, during which the super-hard emission may be absent.

On the other hand, the Suzaku and BeppoSAX (Viotti et al. 2004) results are inconsistent  $\Gamma$ , which may be due to the contamination to the PDS spectra by the neighboring sources (Leyder et al. 2008).

#### 4.2. Origin of the Super-hard Excess Emission

The emission mechanism of the super-hard excess X-rays and the production mechanism of the charged particles (mostly electrons) to produce the radiation are two different problems. For the emission mechanism, we consider the bremsstrahlung and the inverse Compton radiations. The bremsstrahlung emission is either thermal stemming from thermally-relaxed high-temperature plasma or non-thermal from accelerated charged particles with a non-thermal energy distribution.

First, we consider the thermal bremsstrahlung by a thermally-relaxed plasma. In an adiabatic strong shock, the post shock temperature is  $3\mu m_H v_{\text{shock}}^2 / 16k_B$ , where  $\mu$  is the average particle mass in the unit of the proton

mass ( $m_H$ ) and  $v_{\text{shock}}$  is the shock velocity. Substituting  $v_{\text{shock}} = 3000 \text{ km s}^{-1}$  (Pittard & Corcoran 2002), we obtain  $T = 18\mu \text{ keV}$ .  $\mu$  increases for H-deficient gas widely seen among stellar winds from evolved early-type stars such as  $\eta$  Car, and reaches 4/3 for the most extreme case that the gas is composed only of fully-ionized He. The thermal bremsstrahlung model was abandoned in the BeppoSAX (Viotti et al. 2004) analysis and was unemployed in the INTEGRAL analysis (Leyder et al. 2008). The combined Suzaku spectrum indicates  $k_B T^{(\text{br})} > 35 \text{ keV}$ , but given a large systematic uncertainty, we consider that this emission mechanism remains a viable explanation.

Second, we argue against the bremsstrahlung emission by accelerated charged particles colliding upon ambient cold matter. This process is proposed for the super-hard emission seen in solar and stellar flares (Osten et al. 2007).  $\eta$  Car has a rich ambient matter to brake the accelerated particles, which is evidenced by a large amount of circum-stellar extinction and the presence of the FeI fluorescence line (Corcoran et al. 2004). However, the X-ray yield of this process is very low of  $\approx 10^{-5}$  even for the most efficient bremsstrahlung by electrons of a 10 keV to 1 MeV kinetic energy against a thick target. Most of the kinetic energy is lost by the ionization of cold target. The measured luminosity is  $\sim 1 \times 10^{34} \text{ erg s}^{-1}$  in the super-hard band for the two Suzaku observations, which implies that a constant energy input is necessary at a rate of  $\approx 10^{39} \text{ erg s}^{-1}$ . This is hardly possible given the total kinetic energy of the stellar wind in this CWB being  $\sim 10^{37} \text{ erg s}^{-1}$  (Leyder et al. 2008).

Finally, we consider the inverse Compton emission of stellar UV photons by a non-thermal population of electrons scattering the ambient UV photons up to the super-hard band (Chen & White 1991). This is the most popular explanation adopted in Viotti et al. (2004) and Leyder et al. (2008), and our Suzaku result agrees with this interpretation. Several mechanisms of acceleration to produce the non-thermal population are proposed, which includes the first-order Fermi acceleration at the shock, electric field acceleration in the current sheet in a magnetized wind (Jardine et al. 1996), and magnetic reconnections. The X-ray photon index of  $\sim 1.4$  indicates that the injected non-thermal electrons have an energy distribution with an index of  $\sim 2$  or harder, depending on how the Compton cooling balances the injected energy. The diffusive shock acceleration predicts the value of 2 for the electron energy index, and some modifications may need to be considered (Pittard & Dougherty 2006).

The authors acknowledge Y. Hyodo for his help in the XIS data reduction, J. Pittard for his comments on particle acceleration, and J. C. Leyder and R. Walter for providing the INTEGRAL spectrum. We thank the Suzaku science working group team for their effort in the initial phase of the operation, during which the present data set was obtained. Support for this work is provided by the Research Center of the Advanced Measurement at Rikkyo University (A.S.), the Grants-in-Aid for Scientific Research by the Ministry of

Education, Culture, Sports, Science and Technology of Japan (grant numbers 19654032 and 19340047 for S.K. and 20540237 for Y.T.), a Chuo University Grant for Special Research (Y.T.), and the National Aeronautics and Space Administration through Chandra Postdoctoral Fellowship Award Number PF6-70044 (M.T.) issued by the Chandra X-ray Observatory Center, which is operated by the Smithsonian Astrophysical Observatory for and on behalf of the National Aeronautics Space Administration under contract NAS8-03060.

## References

- Aharonian, F., et al. 2007, *A&A*, 467, 1075  
 Albacete Colombo, J. F., Méndez, M., & Morrell, N. I. 2003, *MNRAS*, 346, 704  
 Boldt, E. 1987, *Observational Cosmology*, 124, 611  
 Chen, W., & White, R. L. 1991, *ApJ*, 366, 512  
 Corcoran, M. F., et al. 1998, *ApJ*, 494, 381  
 Corcoran, M. F., et al. 2004, *ApJ*, 613, 381  
 Daminieli, A., et al. 2008, *MNRAS*, 384, 1649  
 Davidson, K., & Humphreys, R. M. 1997, *ARA&A*, 35, 1  
 Evans, N. R., Seward, F. D., Krauss, M. I., Isobe, T., Nichols, J., Schlegel, E. M., & Wolk, S. J. 2003, *ApJ*, 589, 509  
 Evans, N. R., Schlegel, E. M., Waldron, W. L., Seward, F. D., Krauss, M. I., Nichols, J., & Wolk, S. J. 2004, *ApJ*, 612, 1065  
 Fernández-Lajús, E., et al. 2009, *A&A*, 493, 1093  
 Hamaguchi, K., et al. 2007a, *ApJ*, 663, 522  
 Hamaguchi, K., et al. 2007b, *PASJ*, 59, 151  
 Ishibashi, K., Corcoran, M. F., Davidson, K., Swank, J. H., Petre, R., Drake, S. A., Daminieli, A., & White, S. 1999, *ApJ*, 524, 983  
 Ishisaki, Y., et al. 2007, *PASJ*, 59, S113  
 Jardine, M., Allen, H. R., & Pollock, A. M. T. 1996, *A&A*, 314, 594  
 Kaastra, J. S. 1992, *An X-Ray Spectral Code for Optically Thin Plasmas* (Internal SRON-Leiden Report, updated version 2.0)  
 Kokubun, M., et al. 2007, *PASJ*, 59, 53  
 Koyama, K., et al. 2007, *PASJ*, 59, 23  
 Leyder, J.-C., Walter, R., & Rauw, G. 2008, *A&A*, 477, L29  
 Liedahl, D. A., Osterheld, A. L., & Goldstein, W. H. 1995, *ApJ*, 438, L115  
 Luo, D., McCray, R., & Mac Low, M.-M. 1990, *ApJ*, 362, 267  
 Mewe, R., Gronenschild, E. H. B. M., & van den Oord, G. H. J. 1985, *A&AS*, 62, 197  
 Mewe, R., Lemen, J. R., & van den Oord, G. H. J. 1986, *A&AS*, 65, 511  
 Mitsuda, K., et al. 2007, *PASJ*, 59, 1  
 Morrison, R., & McCammon, D. 1983, *ApJ*, 270, 119  
 Nielsen, K. E., Corcoran, M. F., Gull, T. R., Hillier, D. J., Hamaguchi, K., Ivarsson, S., & Lindler, D. J. 2007, *ApJ*, 660, 669  
 Osten, R. A., Drake, S., Tueller, J., Cummings, J., Perri, M., Moretti, A., & Covino, S. 2007, *ApJ*, 654, 1052  
 Pittard, J. M., & Corcoran, M. F. 2002, *A&A*, 383, 636  
 Pittard, J. M., & Dougherty, S. M. 2006, *MNRAS*, 372, 801  
 Serlemitsos, P. J., et al. 2007, *PASJ*, 59, 9  
 Stevens, I. R., Blondin, J. M., & Pollock, A. M. T. 1992, *ApJ*, 386, 265  
 Stevens, I. R., Corcoran, M. F., Willis, A. J., Skinner, S. L., Pollock, A. M. T., Nagase, F., & Koyama, K. 1996, *MNRAS*, 283, 589  
 Takahashi, T., et al. 2007, *PASJ*, 59, 35  
 Takahashi, T., et al. 2008, *Proc. SPIE*, 7011, 18  
 Tsuboi, Y., Koyama, K., Sakano, M., & Petre, R. 1997, *PASJ*, 49, 85  
 Usov, V. V. 1992, *ApJ*, 389, 635  
 Viotti, R. F., et al. 2002, *A&A*, 385, 874  
 Viotti, R. F., Antonelli, L. A., Rossi, C., & Rebecchi, S. 2004, *A&A*, 420, 527  
 White, R. L., & Becker, R. H. 1995, *ApJ*, 451, 352  
 Zhekov, S. A., & Skinner, S. L. 2000, *ApJ*, 538, 808